Chapter 2

Remote sensing of atmospheric water vapour

Most remote sensing techniques of atmospheric properties are based on the modification of radiation by different atmospheric constituents. Atmospheric gases and other constituents leave specific fingerprints in different spectral regions. In case of atmospheric water vapour, the most widely used techniques can be put together in four groups, namely the remote sensing based on

- the absorption of solar radiation
- the emission of infrared radiation (IR)
- the emission of microwave radiation (MW) and
- the path delay of GPS radio signals due to refraction.

In this work, only the first technique is used as it allows accurate measurements over land surfaces with a high spatial resolution. It is based on the absorption of solar radiation in the path sun - surface - sensor. The disadvantage of this method, though, is its high sensitivity to aerosols or thin cirrus clouds. Aerosol layers or thin cirrus clouds can significantly enlarge the photon path in the way from the sun to the sensor through multiple scattering, leading to overestimations of atmospheric water vapour. However, also a reduction of photon path lengths due to backscattering

Table 2.1: Central wavelengths λ, full widths at half maximum δλ and primary use of the MERIS spectral channels

Nr.	λ[nm]	δλ[nm]	Primary use
1	412	10	Yellow substance and detrital pigments
2	442	10	Chlorophyll absorption maximum
3	490	10	Chlorophyll and other pigments
4	510	10	Suspended sediment, red tides
5	560	10	Chlorophyll absorption minimum
6	620	10	Suspended sediment
7	665	10	Chlorophyll absorption & fluo. reference
8	681	7.5	Chlorophyll fluorescence peak
9	708	10	Fluo. reference, atmosphere corrections
10	753	7.5	Vegetation, cloud
11	760	3.75	O_2 R- branch absorption band
12	778	15	Atmosphere corrections
13	865	20	Vegetation, water vapour reference
14	885	10	*Water vapour window channel*
15	900	10	*Water vapour absorption channel*

and consequently shading of lower atmospheric levels is possible, which results in underestimations of water vapour.

In this work, two different satellite instruments are used: the *Medium Resolution Imaging Spectrometer* MERIS on the European Envisat platform and the *Moderate Resolution Imaging Spectroradiometer* MODIS on the U.S.-American TERRA and AQUA satellites. Both instruments are imaging spectrometers, i.e. are taking measurements in 3 dimensions: the first two being the two spatial image dimensions and the third consisting of different spectral channels. MERIS was mainly developed for the remote sensing of ocean constituents but has also dedicated channels for the remote sensing of atmospheric properties. The main difference to MODIS is that the latter also has additional channels in the infrared spectral region, especially allowing a more elaborate remote sensing of clouds and the remote sensing of atmospheric water vapour from emitted thermal radiation. MERIS measurements are made at full resolution of 300 m at nadir direction. This data is available when

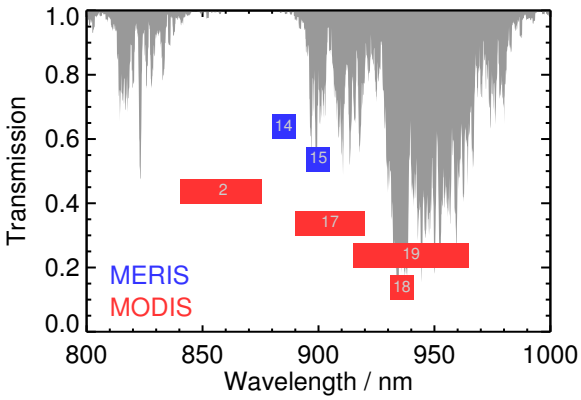

Figure 2.1: Atmospheric transmission of a mid-latitude standard summer atmosphere around the ρστ-water vapour absorption band. The blue and red boxes indicate the spectral location of the MERIS and MODIS channels used for the retrieval of atmospheric water vapour content and the appropriate channel numbers as given in Tables 2.1 and 2.2.

MERIS is in sight from a satellite receiving station only. Globally available reduced resolution data with a nadir resolution of 1 km is created from the full resolution measurements. MODIS measurements are made at three different spatial resolutions: 250 m for channels 1 and 2 (645 nm and 858 nm), 500 m for channels 3 to 7 (469 nm, 555 nm, 1240 nm, 1640 nm, 2130 nm) and 1 km for the remaining channels. The 1 km files include aggregated 1 km resolution measurements of channels 1 to 7. Details about the channel settings and their primary use are given in Tables 2.1 and 2.2.

Envisat was launched $28^{th}$of February 2002 and operational water vapour and other level2 products are available. TERRA is in its orbit since 18^{th} of December 1999 with reliable radiance measurements being available since November 2000. AQUA was launched 4^{th} of May 2002 .

The underlying principle of the differential absorption technique used in this work for the retrieval of atmospheric water vapour and examples of its application to satellite or airborne measurements are published e.g. in [17, 20, 19, 5, 10, 39, 41, 8, 4]. It is generally based on the fact that the intensity of solar radiation in

Table 2.2: Central wavelengths λ, full widths at half maximum δλ and primary use of the MODIS spectral channels

Nr.	λ[nm]	δλ[nm]	Primary use
1	645	50	Land / cloud boundaries
2	858	35	like 1 and *water vapour window channel*
3	469	20	Land / clouds properties
4	555	20	
5	1240	20	
6	1640	24	
7	2130	50	
8	412	15	Ocean colour / phytoplankton / Biogeochemistry
9	443	10	
10	488	10	
11	531	10	
12	551	10	
13	667	10	
14	678	10	
15	748	10	
16	869	15	
17	905	30	*Water vapour absorption channel*
18	936	10	*Water vapour absorption channel*
19	940	50	*Water vapour absorption channel*
20	3750	180	Surface / cloud temperature
21	3959	60	
22	3959	60	
23	4050	60	
24	4465	65	Atmospheric temperature
25	4515	67	
26	1375	30	Cirrus clouds
27	6715	360	Water vapour IR channel
28	7325	300	
29	8550	300	
30	9730	300	Ozone
31	11030	500	Surface / cloud temperature
32	12020	500	
33	13335	300	Cloud top altitude
34	13635	300	
35	13935	300	
36	14235	300	

distinct spectral areas is continuously reduced by absorption by water vapour on its way through the atmosphere. Figure 2.1 shows the transmission of a standard mid-latitude summer atmosphere around the $\rho\sigma\tau$-water vapour absorption band between 900 and 1000 nm and the spectral location of the MERIS and MODIS channels used for the water vapour retrieval. For both instruments, one channel in a spectral region with very high transmission is combined with at least one channel located within the absorption band. In a simplified form, the measured radiance L can be written as a function of incoming solar radiation S_0, atmospheric transmission in the path sun-surface-sensor T and surface albedo α:

$$L \approx S_0 T \alpha. \tag{2.1}$$

The simplifications are that this formulation is true for monochromatic radiation only and that all contributions by scattering in the atmosphere are omitted. Additionally, ignoring any pressure- or height-dependency of absorption coefficients, the monochromatic transmission is an exponential function of the water vapour content. With two channels, one within a water vapour absorption band and one window channel with a transmission equal to 1, the logarithm of the radiance ratio would be a linear function of the columnar water vapour. This last step implicitly introduced two further assumptions, namely that the incoming solar radiation and the surface reflectivity are spectrally constant between the two channels. None of these simplifications is true in reality. Nevertheless, the logarithm of radiance ratios is taken as a mean for the estimation of columnar water vapour but the relationship between both quantities is not a linear function nor analytically derived. Instead, a numerical radiative transfer model [15, 16] was used in this work to simulate satellite radiances for a large variety of atmospheric profiles and surface types. The atmosphere was divided in 21 levels. The vertical dependency of absorption coefficients was calculated monochromatically using the HITRAN molecular spectroscopic database [35, 34]. The radiative transfer model is written for monochromatic radiation, therefore the satellite channels were divided into a number of pseudo-monochromatic subchannels using a modified k-distribution approach [7]. Spectrally varying surface reflectivities were taken from [11], atmospheric profiles of pressure, tempera-

ture and humidity were built from global radio soundings. In total, 1000 simulations were performed for cloud free and cloudy profiles, respectively. The cloudy atmospheric profiles each contained one single-layer cloud. For each profile the cloud type, effective radius, base and top height and optical thickness were chosen randomly from a set of 8 different classes based on the cloud scheme described in [38]. Tropospheric and stratospheric aerosol was added with varying optical thicknesses and accounted for by Mie-theory. In a second step, a regression was performed between the integrated water vapour values known for the simulated profiles and the logarithms of calculated radiance ratios. In a third step, the resulting regression was applied to real satellite measurements for the retrieval of atmospheric water vapour.

Regressions were performed independently for cloud free and cloudy atmospheres, consequently two different water vapour retrieval algorithms were developed for MERIS and MODIS, respectively, for this work. The first allows the remote sensing of integrated columnar water vapour above cloud free land surfaces, the second is designed for the retrieval of water vapour in cloudy atmospheres, here, the integrated water vapour from top of the atmosphere down to the cloud top is derived[1]. The first algorithm is based on the work described in [8], the second is an extension of the author's work already published in [4].

Modifications of the existing algorithms include the usage of the latest line-by-line absorption coefficients, the extension from MERIS to MODIS and the usage of a neural-network based retrieval technique instead of multi-dimensional quadratic polynomial regression. While for MERIS this was done mostly for the simplicity of the algorithm application to satellite measurements, this approach allowed for MODIS the simultaneous use of measurements in different absorption channels. Later in this chapter it will be shown how this reduces the retrieval error due to the unknown surface reflectivity in the different channels.

The following section contains the results from a validation of water vapour absorption coefficients published in different molecular spectroscopic databases. In the next section a sensitivity study and a study on the advantage of the concurrent

[1] In this work, a number of expressions is used synonymously for the denotation of the columnar integrated water vapour content, e.g. water vapour, water vapour content, integrated water vapour, columnar water vapour, precipitable water. In the literature, different units of this quantity are used. A table with the units and the appropriate conversion factors is given in the appendices on page 79.

use of the different MODIS water vapour absorption channels is shown together with the expected theoretical retrieval accuracy of the algorithms based on the radiative transfer simulations. Finally, the application of the derived method to satellite data is shown.

2.1 Line absorption

Many remote sensing techniques for the retrieval of atmospheric properties are based on radiation measurements. An important prerequisite for accurate results is precise knowledge about the radiative properties of gaseous absorption. Water vapour strongly absorbs solar radiation, and the physical details like line intensities and broadening coefficients are collected (for various atmospheric gases) in molecular databases such as HITRAN [35, 34], GEISA [32] and ESA-WVR[36]. These databases result from a mixture of laboratory measurements as well as theoretical calculations. Errors in the databases will always lead to false estimates of atmospheric transmission and consequently to erroneous retrieval results. Therefore, their accuracy has to be investigated carefully, especially, since the databases have undergone continuous modifications and improvements [23, 12]. A validation of the HITRAN and ESA-WVR databases for the near-infrared spectral range with respect to absorption by water vapour was performed for this work using spectrally highly resolved clear-sky ground-based measurements of direct solar radiation.

These measurements were performed by Kevin Smith at the Rutherford Appleton Laboratory (UK) on 20 August 1999 using a high-resolution Bomem DA3.002 Fourier transform spectrometer. A description of this instrument can be found in [37]. It measures the relative intensity of direct solar radiation (in arbitrary units) transmitted through the atmosphere. For the comparison, simulated spectra were calculated for the three HITRAN databases HITRAN-96, HITRAN-99 and HITRAN-2000 and for ESA-WVR using the Reference Forward Model version 4.12 [14]. The model atmosphere necessary for these simulations was compiled from ECMWF[2] operational data for altitudes below 30 km and from a mid-latitude

[2]European Centre for Medium-Range Weather Forecasting

summer standard atmosphere for altitudes above. The ECMWF data is supplied at constant pressure levels on a 2.5° grid, from which temperature and water vapour concentration profiles were interpolated spatially and temporally along the line-of-sight of the measurements. The resulting total precipitable water vapour was 17.9 mm. The uncertainty of this value was estimated from comparisons with UKMO[3] radiosonde measurements. For this purpose, the ECMWF data was interpolated to the time and position of the radiosonde ascents. The resulting uncertainty in columnar water vapour was $\pm 6\%$.

The measured relative intensities $I(\upsilon)$ at each wavenumber ν (in cm^{-1}) were converted to pseudo-optical depths $s'_{meas}(\nu)$ by

$$s'_{meas}(\nu) = -\ln\left(\frac{I(\nu)}{I_{max}}\right), \tag{2.2}$$

where I_{max} is the maximum signal (in arbitrary units). The pseudo-optical-depth spectrum was then modeled for 100 cm^{-1} wide intervals between 10150 and 11250 cm^{-1} (889 - 985 nm) using a Marquardt non linear least-squares fit and the calculated spectra $s_{calc}(\tilde{\nu})$, where $\tilde{\nu}$ was the wavenumber grid (in cm^{-1}) of the calculations. Additional fits were performed separately for the MERIS water vapour absorption channel and the water vapour absorption channel of the *Modular Optoelectronic Scanner* MOS[4] [43, 42] centered around 945 nm (10582 cm^{-1}).

For each spectral interval the state vector of the Marquardt forward model $s_{calc}(\nu)$ consisted of

- a scaling factor f for the optical depth, allowing corrections of the spectral line intensities,
- an absolute wavenumber shift $\delta\tilde{\nu}$ that mapped $\tilde{\nu}$ onto ν, allowing a correction of spectral misalignments of lines and

[3] United Kingdom Meteorological Office

[4] The MOS instrument was used in this work as a precursor for MERIS in the time before MERIS data became available. MOS is a development of the German Aerospace Center DLR, launched in March 1996 on the Indian IRSP-3 platform. It is equipped with one water vapour absorption channel at 945 nm and one window channel at 865 nm. The spatial resolution is 500 m, but the swath width is only 200 km.

- a wavenumber-independent zero transmission offset τ_{dc}, accounting for any small intensity offset in the recorded spectra possibly caused by instrumental effects. This offset was determined from signal levels outside of the optical bandpass of the instrument and from opaque regions of the spectrum.

- Finally, the state vector contained the coefficients a_i of a fourth-order polynomial function, representing the effective"top of the atmosphere" background signal $s_0(\nu)$.

The latter was necessary, as the measurements were not radiometrically calibrated. Therefore, an effective background spectrum representing the signal that would be observed at the top of the atmosphere had to be determined. As this approximation can not simulate solar absorption, spectral regions affected by solar absorption lines were identified using the Kurucz solar spectrum [27] and excluded from the fits. The determined background spectrum also contained the envelope of the spectral response of the instrument and contributions from the water vapour continuum, as these are devoid of any sharp spectral structure and were consequently effectively included in the fitted polynomials. The mathematical description of the forward model is as follows:
spectral shift:

$$\nu = \tilde{\nu} + \delta\tilde{\nu}, \tag{2.3}$$

effective background spectrum:

$$s_0(\nu) = \sum_{i=0}^{4} a_i \nu^i, \tag{2.4}$$

forward model:

$$s_{calc}(\nu) = -\ln\left[\exp\left(-\left(f\, s_{calc}(\nu) + s_0(\nu)\right)\right) + \tau_{dc}\right], \tag{2.5}$$

such that

$$s_{calc}(\nu) \cong s'_{meas}(\nu), \tag{2.6}$$

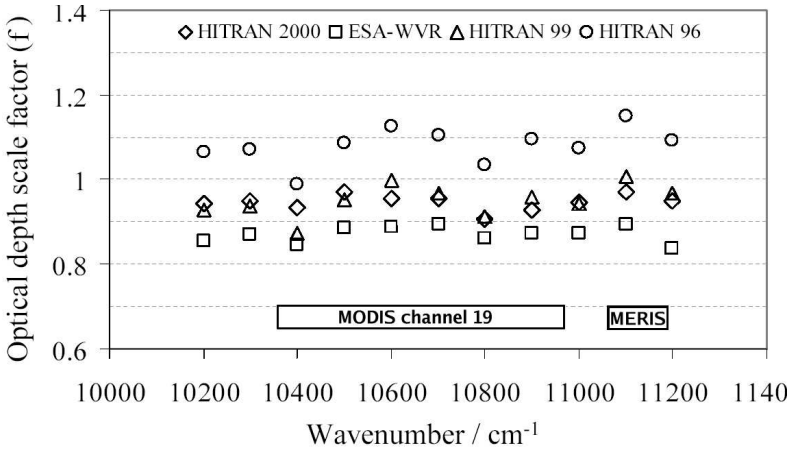

Figure 2.2: Optical depth scaling factors f determined from observed and calculated integrated intensities over 100 cm^{-1} wide spectral intervals for four different databases. The spectral range of the MERIS and MODIS water vapour absorption channels 14 and 19, respectively, are indicated.

i.e. the fit was performed such that the least-square differences between the forward model and the pseudo-optical depth spectrum were minimised. The actual result of the Marquardt fit are the scaling factors, the wavenumber shift, the transmission offset and the background signal for each 100 cm^{-1} wide spectral interval with which the measurements can best be reproduced by the simulations. With these values, the measured optical depth can be calculated from the pseudo-optical depth by subtracting the background signal and correcting for the wavenumber shift and the transmission offset:

$$s_{meas}(\tilde{\nu}) = -ln\left[\exp\left(-s'_{meas}(\nu - \delta\tilde{\nu})\right) - \tau_{dc}\right] - s_0(\tilde{\nu}). \tag{2.7}$$

The resulting optical depth scaling factors are illustrated in Figure 2.2 for the HITRAN 2000, ESA-WVR, HITRAN 98 and HITRAN 96 databases. The HITRAN 2000 and HITRAN 99 databases show the highest accuracy, while the ESA-WVR and HITRAN-96 database significantly over- and underestimate absorption by water vapour.

The quality of the non linear least-square fit and the forward model, especially

Table 2.3: Relationships between integrated optical depth scaling factors. Values in the first row (1) are from [6], values in the second row (2) are from this work.

	HITRAN 99		HITRAN 96		ESA-WVR	
	1	2	1	2	1	2
HITRAN 99	1.00	1.00	0.88	0.88	1.06	1.07
HITRAN 96	1.14	1.13	1.00	10.0	1.21	1.21
ESA-WVR	0.94	0.94	0.83	0.83	1.00	1.00

the determination of the background function and the scaling factors, was indirectly investigated by the comparison of the ratios between calculated optical depth scaling factors from different databases with the results from a similar study previously carried out by [6] for HITRAN 99, HITRAN 96 and ESA-WVR. In this study, scaling factors between the databases were calculated for one spectral interval covering the whole water vapour absorption band in the range from 10100 to 11200 cm^{-1} (892 - 990 nm). In Table2.3 the results are compared to the appropriate scaling factors calculated in this work for the MOS absorption channel .

The agreement better than 1% suggests that the procedure used here has not introduced any significant database-dependent artefacts to the inter-comparison.

As the measured optical depth spectrum (2.7) is on the wavenumber grid of the simulations ($\tilde{\nu}$), both can be compared and the quality of each fit is expressed in terms of observed-minus-calculated residual spectra and values of the ratio of simulated and measured integrated optical depths *Rs*:

$$R_s = \frac{\int_{\tilde{\nu}_1}^{\tilde{\nu}_2} s_{meas}\,(\tilde{\nu})\,\mathrm{d}\tilde{\nu}}{\int_{\tilde{\nu}_1}^{\tilde{\nu}_2} f\, s_{calc}\,(\tilde{\nu})\,\mathrm{d}\tilde{\nu}}. \tag{2.8}$$

Figure 2.3 shows for all four databases the relative deviation of observed - (unscaled) calculated optical depths as a function of observed optical depth for the MOS absorption channel. The deviation is shown as a two-dimensional histogram of the number of occurrences for each pair of observed optical depth and relative difference. The logarithmic scale is used to account for the dynamic range of the total number of observations for different optical depths. The white crosses

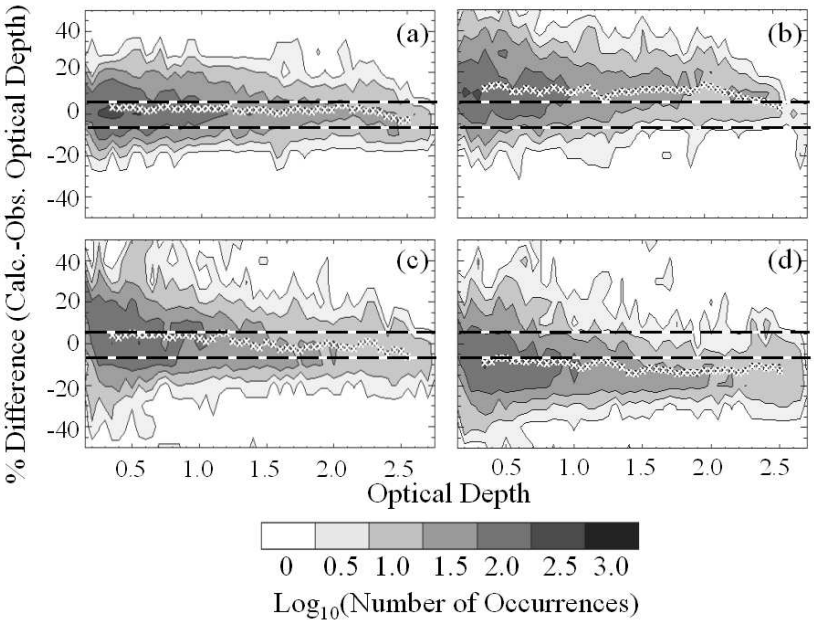

Figure 2.3: Two dimensional histograms of the relative difference between calculated and observed optical depths for the a) HITRAN 2000, b) ESA-WVR, c) HITRAN 99 and d) HITRAN 96 database for a spectral interval around 940 nm (10638 cm^{-1}). The white crosses represent the mean values of the distribution at increments of 0.05 in optical depth. The dashed horizontal lines indicate the extremes resulting from the estimated $\pm$ 6% uncertainty on the water vapour total column.

represent the mean of the number distribution for individual 0.05 wide intervals of optical depth. The HITRAN 2000 database shows the best agreement between calculations and observations, with a mean deviation smaller than the estimated uncertainty arising from the $\pm$ 6% uncertainty on the water vapour total column used in the calculations of the simulated spectra. The same is true for HITRAN 99, however, the spread of the distribution is wider. This is partly due to the misassignment of intensity between pairs of absorption lines, leading to larger but compensating residuals.

Consequently, the HITRAN 2000 database was used in all radiative transfer simulations for this work.

2.2 Sensitivity studies and error analysis

A sensitivity study was performed for the retrieval algorithms for water vapour above land based on the simulation results used for the algorithm development. The purpose was to calculate the expected sensitivity of both satellite instruments to variations in the columnar water vapour content and to estimate the expected errors due to sensor noise. As the radiance ratio between one absorption and one window channel is used as an approximation of the transmission in the absorption channel, the negative logarithm of the radiance ratio was related to the columnar water vapour content. Let this parameter be the signal s:

$$s = -ln\left(\frac{L_{abs}}{L_{win}}\right), \tag{2.9}$$

then the sensitivity ζ is defined as follows:

$$\zeta = \frac{\partial s}{\partial PWV\, s} \cdot 100 \left[\frac{\%}{mm}\right], \tag{2.10}$$

where PWV denotes the precipitable water vapour. The sensitivity was calculated for MERIS and MODIS from the results of the radiative transfer simulations, for the latter, different combinations of absorption and window channels were used. The results for a nadir viewing angle and a sun zenith angle of 35° are illustrated in

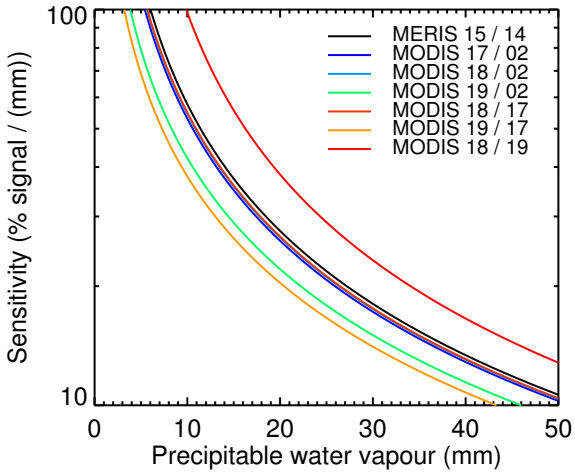

Figure 2.4: Sensitivity of the measured signal for varying columnar water vapour content above land. The signal is the logarithm of the radiance ratio of one absorption and one window channel. Value are calculated for nadir viewing direction and sun zenith angle of 35°.

Figure 2.4. One can see, that for all channel combinations, the relative sensitivity decreases significantly with increasing water vapour. The sensitivity for MERIS is well within the range of the different possible MODIS channel combinations. However, this result has to be seen in combination with the signal-to-noise ratio of the different channels, as a signal inaccuracy of Δs due to the sensor noise will lead to an estimated inaccuracy in the derived water vapour of $\Delta PWV = \frac{\Delta s}{s\zeta}$. For an estimation of this error, measurements of the MODIS signal-to-noise ratios were taken from [2], for MERIS, the signal-to-noise ratio as given in [9] is 1650 at 412.5 nm for a typical ocean signal. However, the signal-to-noise-ratio decreases towards the NIR and a value of 300 was chosen for the MERIS water vapour channels (Rene Preusker, personal communication). The signal-to-noise-ratios for all channels are given in Table 2.4. Assuming these signal-to-noise ratios, the estimated uncertainty in the signal s and the resulting uncertainty in derived water vapour were also calculated from the simulations and are illustrated in Figure 2.5. For most of the channel combinations, the relative error is below 4 % for precipitable water vapour values

Table 2.4: Signal-to-noise ratios of the different MERIS and MODIS water vapour absorption and window channels used for the estimation of retrieval error due to sensor noise.

Instrument	Channel number	Signal-to-noise ratio
MERIS	14	300
MERIS	15	300
MODIS	2	500
MODIS	17	400
MODIS	18	100
MODIS	19	500

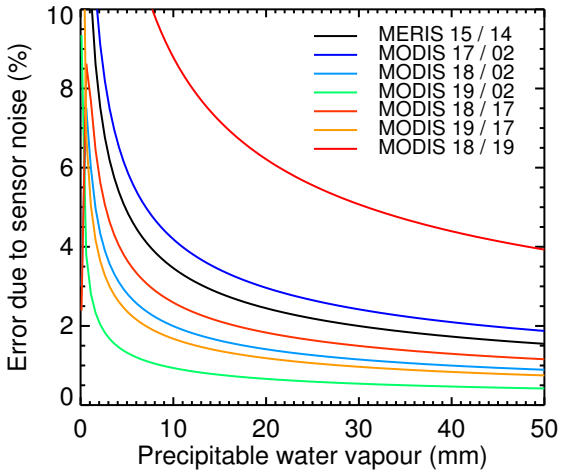

Figure 2.5: Estimated relative error in columnar water vapour content due to sensor noise. Values are calculated for nadir viewing direction and sun zenith angle of 35°.

higher then 10 mm, only the use of MODIS channels 18 and 19 shows significantly larger errors.

However, Sensor noise is not the only source of errors in the retrieved water vapour values, in fact, they are significantly exceeded by errors due to the spectral variability of the surface reflectivity or due to varying atmospheric aerosol loading [8]. This is illustrated in Table 2.5, where the root mean square errors resulting from quadratic polynomial regressions for the individual two-channel combinations are given for 20.000 randomly chosen simulations with sun zenith angles between 12° and 70° and viewing zenith angles of 0° and 50°. Also shown are the results from two different neural-network based retrieval methods.

The two MERIS channels are located close to each other, therefore the effects of spectral variations of the surface reflectivity are smaller than for MODIS, leading to a smaller error. Although each individual regression for MODIS shows comparably high errors, the combination of the different radiance ratios in one algorithm can significantly reduce the overall error. In the original MODIS water vapour algorithm, this is achieved by a weighted average of the water vapour values retrieved from different channels [21]. From this method, the authors expect an accuracy of 13%, which would, for the mean water vapour value of the simulations used in Table 2.5, correspond to a rmse of 3.1 mm.

A different approach is followed here. A neural-network based approach was chosen to incorporate the effects of varying surface reflectivity. A positive side-effect of this is that the neural network delivers water vapour estimates for all possible viewing geometries without the need for multi-dimensional interpolation associated with the use of look-up tables. Two different neural networks were trained for MODIS: one using only one radiance ratio (of channels 18 and 2) and the ratio of surface reflectivities between these two channels, the other using 4 radiance ratios (17/2, 18/2, 19/2, 18/17) but no information about the surface. Both networks also had the sun and viewing geometry as input. The theoretical regression accuracy for both methods is also given in Table 2.5. It is clear that inclusion of information about the slope of surface reflectivity significantly improves the quality of the regression. However, for practical application, this approach requires accurate albedo information for each pixel under varying illumination geometries, for

Table 2.5: Root mean square errors of retrieved columnar water vapour above land from simulated radiances. For details, see text.

Instrument	Absorption channel	Window channel	rmse [mm]	rel. rmse [%]
MERIS	15	14	2.3	9.7
MODIS	17	2	4.7	19.8
MODIS	18	2	2.9	12.2
MODIS	19	2	4.5	19.0
MODIS	18	17	3.0	12.7
MODIS	19	17	5.5	23.0
MODIS	18	19	4.7	19.9
MODIS	neural network using two channels and surface reflectivity ratio		2.5	10.6
MODIS	neural network using different channels		2.7	11.4

different seasons, etc. It is also clear that the simultaneous use of different channel ratios without further information about the surface reflectivity can partly fill the gap. The regression accuracy of this method is between the results from the best performing simple quadratic regression and the neural network approach for one channel ratio and surface information.

As a result, this neural network approach was used for MODIS for the following work. For MERIS, also a neural network approach was chosen. This was not done for the purpose of higher regression accuracy but for the simplicity of its application. The theoretical retrieval accuracy of both neural networks with regard to the simulations is illustrated as a function of sun and viewing geometry in Figure 2.6. The results are based on the same randomly chosen subset of simulations described above. No significant dependency of the regression error on the sun and viewing zenith angles exists, despite an increase for large sun zenith angles. It has to be mentioned that the errors for both instruments increase significantly for sun zenith angles $> 75^\circ$ (not shown). The overall error for MERIS is slightly smaller than for MODIS.

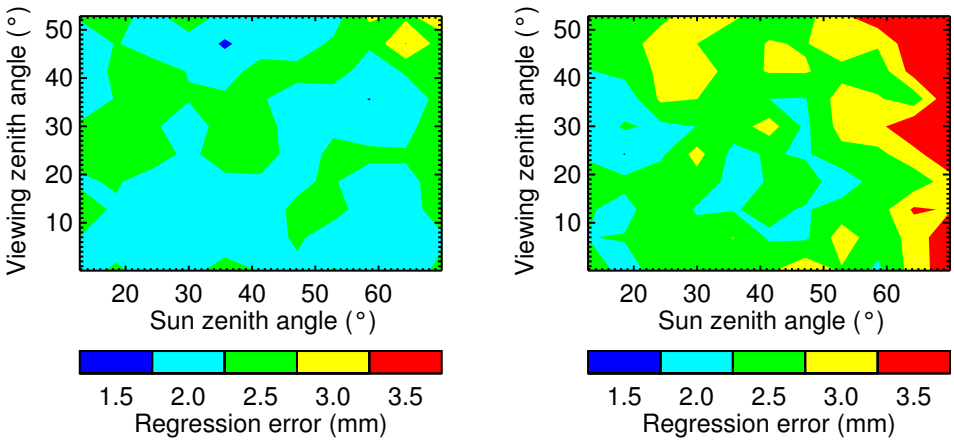

Figure 2.6: Theoretical regression error for water vapour above land based on the inversion of simulated radiances. Results are shown as a function of sun and viewing geometry for MERIS (left panel) and MODIS (right panel). Inversions were performed for 20.000 randomly chosen simulations with sun zenith angles between 12° and 70° and viewing zenith angles of 0° and 50°.

The opposite behaviour can be observed for water vapour above clouds. In [4] it was mentioned that for MERIS the regression accuracy can be expected to increase slightly with increasing viewing zenith angle. This is due to the fact that with increasing air mass the optical thickness in the path sun-cloud-sensor also increases, reducing the fraction of measured radiation that penetrated through the cloud and was reflected at the surface. Generally the regression accuracy decreases for increasing surface reflectivity and decreasing cloud optical thickness. The accuracy's dependency on air mass was further investigated here using the results from the radiative transfer simulations. In Figure 2.7, similar plots are shown as in the previous Figure, here the regression error was calculated from 20.000 simulation results in cloudy atmospheres, with a maximum surface albedo of 0.3. It is well visible that the regression accuracy for both instruments generally increases with increasing air mass, and that the retrieval accuracy for MODIS is significantly higher than for MERIS (note the different range in the two panels). Here the fact that the atmospheric transmission in the 3 MODIS water vapour absorption channels is different seems to be advantageous for the retrieval.

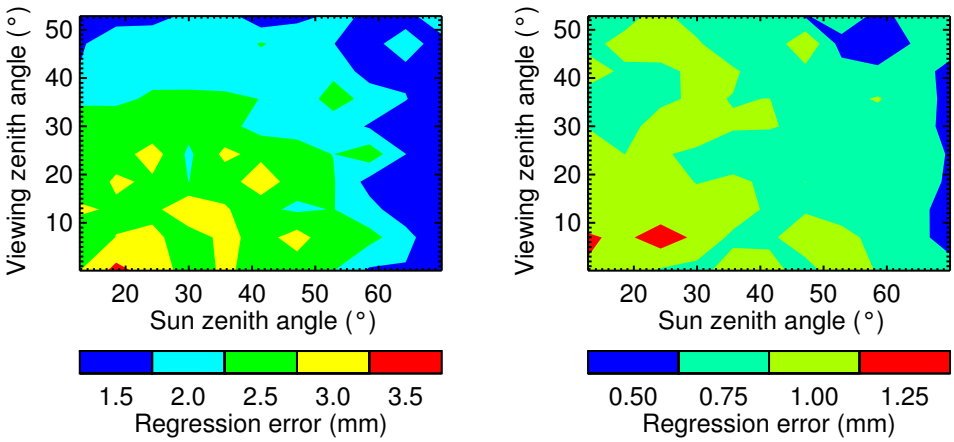

Figure 2.7: Theoretical regression error for water vapour above clouds based on the inversion of simulated radiances. Results are shown as a function of sun and viewing geometry for MERIS (left panel) and MODIS (right panel). Inversions were performed for 20.000 randomly chosen simulations with sun zenith angles between 12° and 70°, viewing zenith angles of 0° and 50° and surfaces reflectivities $\leq$0.3.

2.3 Application to satellite measurements

In this section, examples of the successful application of the developed algorithms to satellite measurements are presented. The first example is based on MERIS full resolution level1b data, the measurements being taken 12th of August 2003 over Spain. Figure 2.8 shows a true colour image of the entire scene covering a large part of the Spanish peninsula. The image shows an almost cloud free scene. In Figure 2.9, a subset of this image is shown, namely the confluence of two rivers, Rio Jarama and Rio Tajuna. From the measured radiances, atmospheric water vapour was derived using the algorithm described above and the result is shown in the same Figure, together with the surface height taken from the GTOPO30 digital elevation model [1]. The river valleys are always lower than the surrounding land and the air above the water surface can be expected to contain more atmospheric humidity, both facts leading to increased columnar water vapour values. This is well represented in the water vapour field, where the derived water vapour increases close to the river beds.

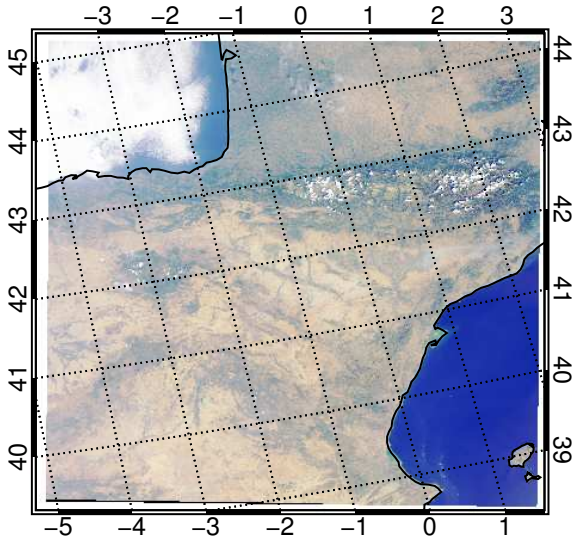

Figure 2.8: True colour image created from MERIS full resolution measurements taken 12.08.2003.

The dependency of columnar water vapour on height is also illustrated in the next example taken 3rd of August 2002 over Sicily. Here, MERIS reduced resolution level1b data was converted into atmospheric water vapour. Figure 2.10 shows the true colour image of this scene, the derived water vapour, the surface height and a transection of surface height and water vapour along 15°E. It is well visible that

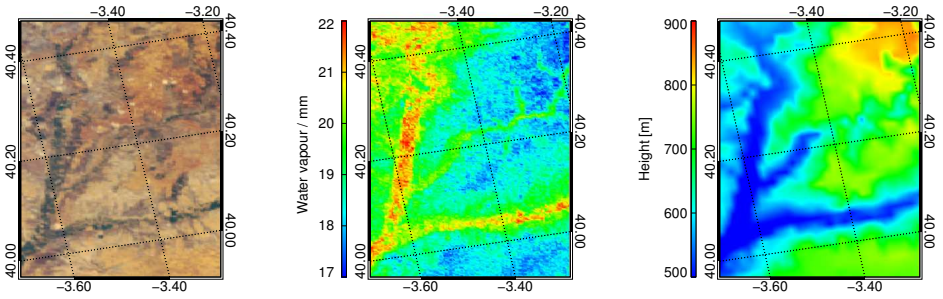

Figure 2.9: Subset of the MERIS scene shown above (left), derived columnar water vapour (middle) and surface height from a digital elevation map (right)

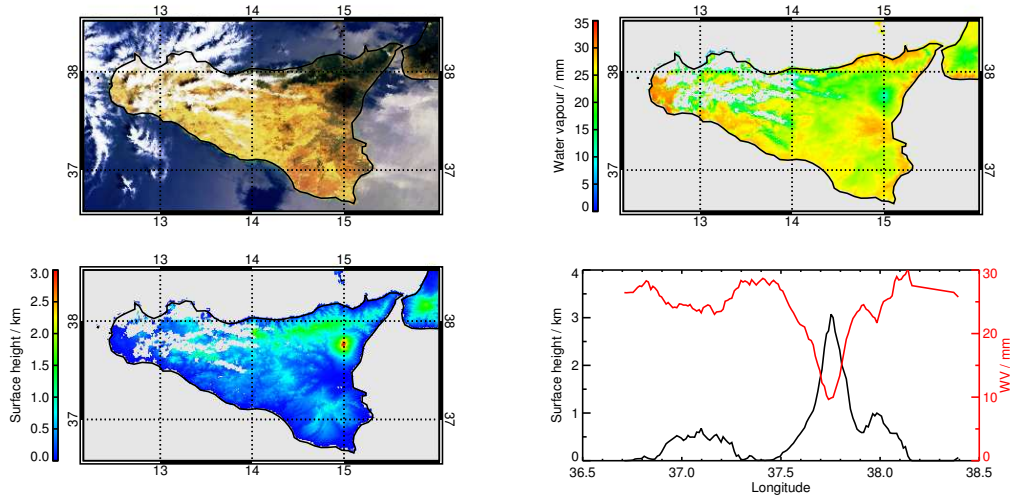

Figure 2.10: MERIS reduced resolution scene taken the 3rd of August 2002 over Sicily. Shown are a true colour image (upper left), the derived integrated water vapour (upper right), the surface height (lower left) and a transection of surface height and water vapour along 15°E (lower right).

with increasing surface height, the derived integrated water vapour decreases.

In the next example, the algorithm for the retrieval of columnar water vapour above clouds is applied to a cloudy scene of MERIS reduced resolution data taken 12th of December 2002 over eastern Germany and Poland. In Figure 2.11, similar Figures as above are shown, with the surface height replaced by retrieved cloud top pressure derived using the algorithm described in [18]. The scene is clearly divided in two parts with low cloud top pressure in the northern and higher cloud top pressure in the souther part. However, the retrieved integrated water vapour from top of the atmosphere down to the cloud top is comparably low over both the low clouds in the northern and the high clouds in the southern part. This behaviour can easily be explained with a NCEP reanalysis of 850 hPa temperature valid for 00 UTC this day. The original image is taken from http://www.wetterzentrale.de/topkarten, a subset is shown in Figure 2.12. A strong front is visible with the strongest temperature gradient lying right in the middle of the area covered by the MERIS scene. North of the front, temperatures are much lower than in the South. The cold air can carry much less humidity, therefore the integrated water vapour here is much

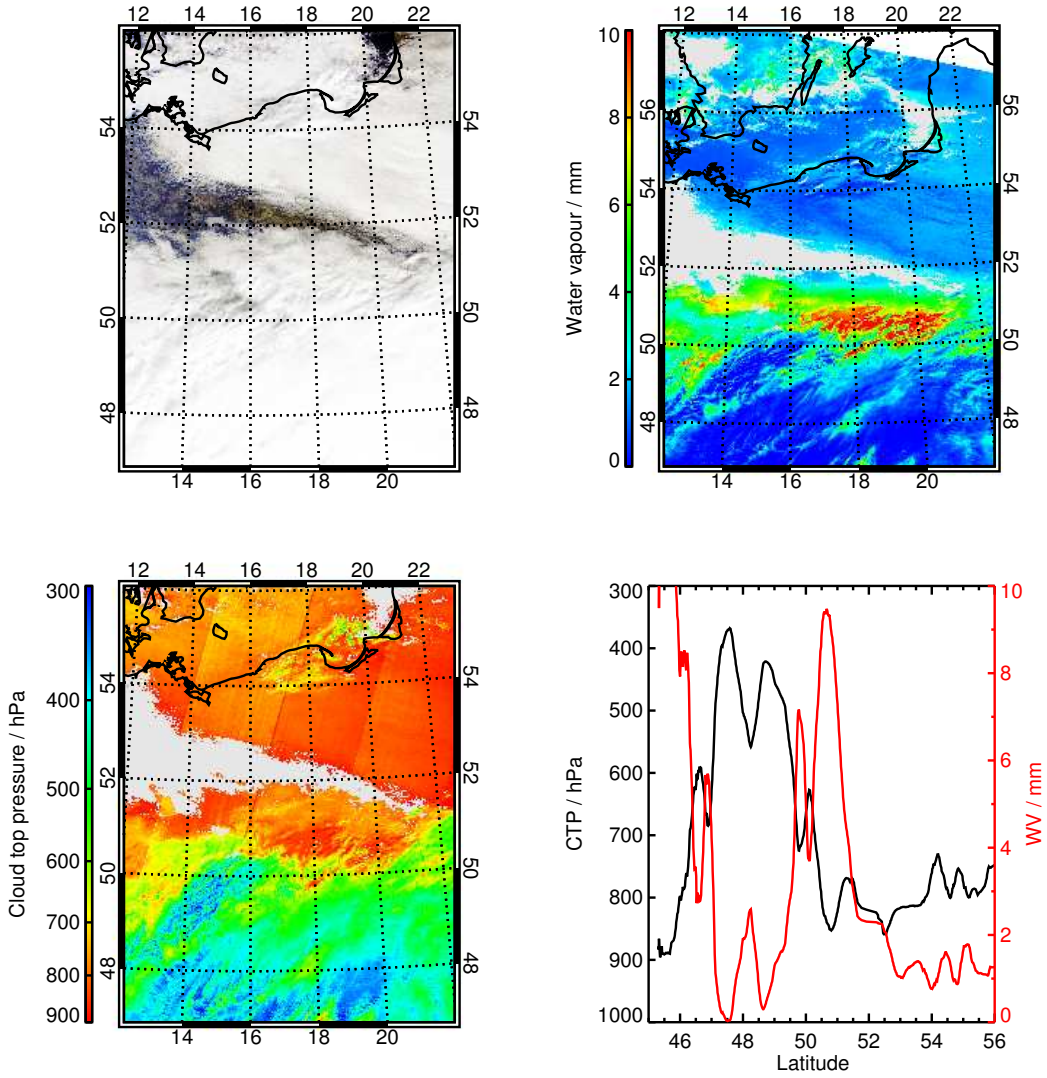

Figure 2.11: MERIS reduced resolution scene taken the 12th of December 2002 over eastern Germany and Poland. Shown are a true colour image (upper left), the derived integrated water vapour above clouds (upper right), the derived cloud top pressure (lower left) and a transection of cloud top pressure and water vapour along 18°E (lower right).

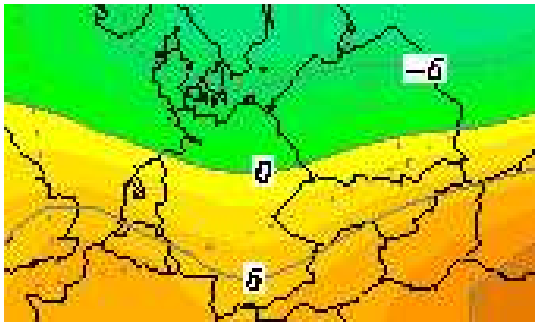

Figure 2.12: NCEP reanalysis of 850 hPa temperature for 12. 10. 2002, 00 UTC. Figure taken from http://www.wetterzentrale.de/topkarten

lower although the clouds are much closer to the ground. In the southern part of the image, the warmer air carries more humidity, however, most of the clouds are much higher and only a small portion of the full atmospheric columnar water vapour is "visible" to the satellite. . The transection in Figure 2.11 also indicates the location of the front around 53°N. Over the whole transection, the integrated water vapour is generally as expected anti-proportional to the cloud top pressure. However, while the cloud top pressure remains roughly around 800 hPa between 50°N and 54°N, the columnar water vapour above the clouds drops from a peak value close to 9 mm down to values smaller than 2 mm.

The last example shows the columnar water vapour above land retrieved from a MODIS scene taken the 6th of August 2003 over central Europe. In Figure 2.13 it is well visible that due to the larger viewing angle MODIS is covering a much larger area during each overpass than MERIS. Two areas with remarkably high water vapour values can be seen in this scene at the western border of France and in the valley of the river Po in Italy. There is also thin dust visible along the middle eastern image boundary which might influence the water vapour retrieval. For a quick comparison, the retrieved water vapour was compared to 6 radio soundings, which are indicated in the above Figure as crosses. The scatter plot for these 6 cases shows a good agreement, the high water vapour values are likely to be no retrieval artefacts.

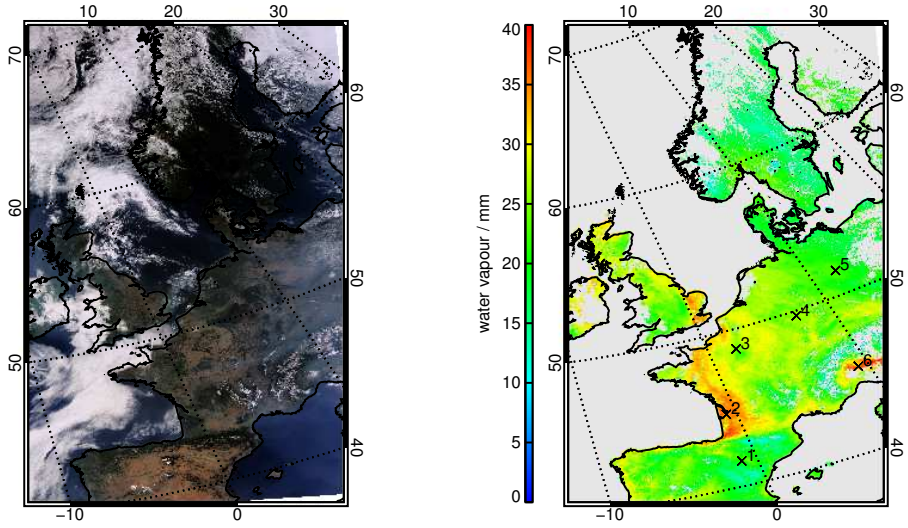

Figure 2.13: True colour image and retrieved water vapour from a MODIS scene taken the 6th of August 2003.

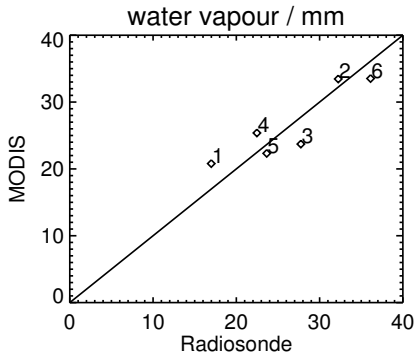

Figure 2.14: Columnar water vapour from radio soundings and MODIS for the radiosonde station indicated in figure 2.13.